DOI: 10.15825/1995-1191-2021-4-132-142

COMPUTER MODELING OF DIFFERENT SHAPED PATCHES IN CLASSICAL CAROTID ENDARTERECTOMY

V.G. Borisov[1, 2], Yu.N. Zakharov[1, 2], A.N. Kazantsev[3], Yu.I. Shokin[1, 2], A.V. Evtushenko[4], L.S. Barbarash[4], P.S. Onishchenko[2, 4], K.Yu. Klyshnikov[4], E.A. Ovcharenko[4]

[1] Kemerovo State University, Kemerovo, Russian Federation
[2] Federal Research Center for Information and Computational Technologies, Novosibirsk, Russian Federation
[3] City Alexandrovskaya Hospital, St. Petersburg, Russian Federation
[4] Research Institute for Complex Problems of Cardiovascular Diseases, Kemerovo, Russian Federation

Objective: to construct geometric models of carotid bifurcation and build a computer modeling for carotid endarterectomy (CEA) operations with patches of various configurations. **Materials and methods.** The method uses reconstructed models of a healthy blood vessel obtained from a preoperative computed tomography (CT) study of the affected blood vessel of a particular patient. Flow in the vessel is simulated by computational fluid dynamics using data from the patient's ultrasonic Doppler velocimetry and CT angiography. Risk factors are assessed by hemodynamic indices at the vessel wall associated with Wall Shear Stress (WSS). **Results.** We used the proposed method to study the hemodynamic results of 10 virtual CEA operations with patches of various shapes on a reconstructed healthy artery of a particular patient. The reason for patch implantation was to ensure that the vessel lumen is not narrowed as a result of the surgery, since closing the incision without a patch can reduce the vessel lumen circumference by 4–5 mm, which adversely affects blood flow. On the other hand, too wide a patch creates aneurysmorphic deformation of the internal carotid artery (ICA) mouth, which is not optimal due to formation of a large recirculation zone. In this case, it was found that the implanted patch width of about 3 mm provides an optimal hemodynamic outcome. Deviations from this median value, both upward and downward, impair hemodynamics. The absence of a patch gives the worst of the results considered. **Conclusion:** The proposed computer modeling technique is able to provide a personalized patch selection for classical CEA with low risk of restenosis in the long-term follow-up.

Keywords: classical carotid endarterectomy, computer modeling, patch.

INTRODUCTION

Acute cerebrovascular accident due to hemodynamically significant stenosis of the internal carotid artery (ICA) is one of the main causes of death and long-term disability [1, 2].

Classical carotid endarterectomy (CEA) is one of the most common treatment options for this patient cohort [1, 2]. However, as a result of patch implantation during this intervention, local deformation of the vessel may occur, leading to changes in flow hemodynamics.

The study of hemodynamic characteristics of blood flow on the vessel wall is extremely difficult in vitro, and even more so in vivo.

Therefore, computational methods of hydrodynamics are widely used to assess hemodynamic effects in vessels of a personally-specific shape [3, 4].

The aim of the work is to identify the zones of the highest risk of restenosis in the constructed computer models during classical CEA.

MATERIALS AND METHODS

Initial mathematical modeling data

The initial geometric model of the vessel was reconstructed based on preoperative computed tomography (CT) of the affected left carotid bifurcation of a particular patient. Fig. 1 (a) shows the affected part of the vessel flow area (the carotid artery is in the foreground). The segment of the curve in Fig. 1 (a) shows the presumed position of the vessel wall beneath the atherosclerotic plaque. The dotted line marks the inner surface of the plaque in the depicted projection.

The initial flow modeling data are the results of postoperative ultrasound Doppler velocimetry (UDV) of the patient. The dependence of inlet flow velocity on time was plotted on the basis of UDV study of the common carotid artery (CCA). The ratio of flow rates through the internal carotid artery (ICA) and external carotid artery (ECA) was calculated using their cross-sectional areas

Corresponding author: Anton Kazantsev. Address: 4, Solidarity Avenue, St. Petersburg, 193312, Russian Federation. Phone: (908) 947-47-57. E-mail: dr.antonio.kazantsev@mail.ru

and time-averaged peak velocity (TAPV), which were also derived from UDV data.

Building geometric models

A reconstructed 3D model of a healthy vessel was built using SimVascular Updegrove (2016) and Salome Salome (2007) software. SimVascular was used to construct vessel segments (see Fig. 1 (b–d)). Using a Python script of our own design, these segments were then imported into Salome to build the geometric model and grids. The reconstructed 3D model of the vessel is shown in Fig. 1 (e). This model is referred to hereafter as the base model and is denoted by m0. The black line on the vessel wall in Fig. 1 (e) indicates the incision line for subsequent simulation of patch implantation.

The above script was also used to visually model the result of CEA surgery. It can be used to visually draw the incision line and the patch contours on the vessel segmentation contours (see Fig. 2). Information about the drawn lines is exported by the script to a data file as a list of patch width values at its intersections with segmentation contours. The script then uses this data to change the geometric shape of the base model, simulating the patch implantation result.

The modified models, which are the results of virtual CEA, were constructed by increasing (or decreasing) the perimeters of all model segments m0 that intersect the incision line. This allows to simulate any shape of the patch or incision closure without a patch. Perimeters were changed by scaling the segments relative to their geometric centers according to the values recorded in the data file. The default scaling factor is assumed to be equal to the value of the relative perimeter increment stored in the file, divided by 2π. For segments close to ellipses

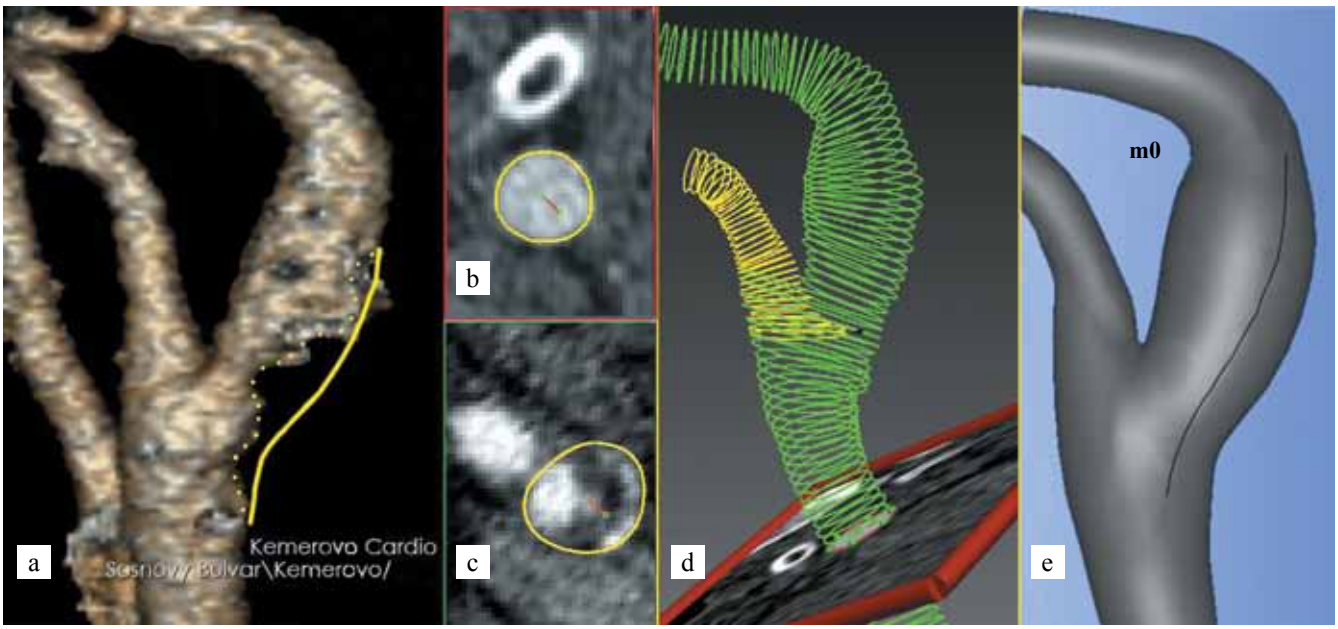

Fig. 1. CT angiography of preoperative flow area in carotid arteries (vessel in the foreground). (a) Segmentation contour in the healthy part of the CCA. (b) Segmentation contour in the affected part of the ICA near the bifurcation. (c) CCA-ICA and ECA segmentations. (d) Geometric shape of the base model m0 with an incision line (e)

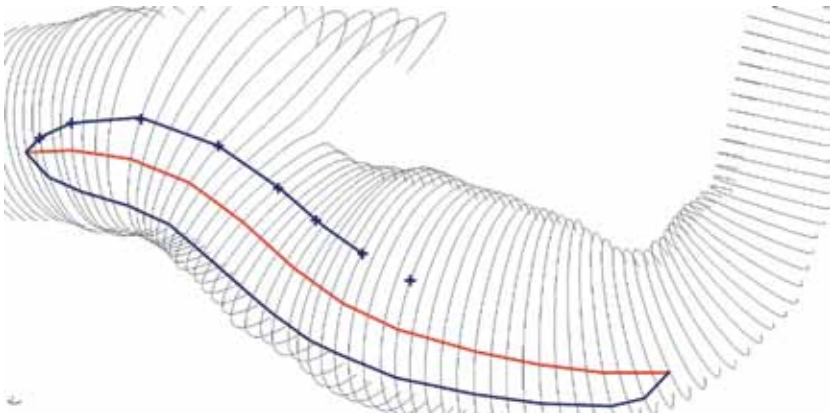

Fig. 2. The process of visual construction of the patch shape on the CCA-ICA segmentation contours

with small eccentricity, this choice is accurate enough. For irregularly shaped segments, the scaling factor can be adjusted manually if desired. Due to scaling, the upper (in Fig. 2) parts of the ICA proximal contours were shifted upwards and began to intersect with the ECA proximal contours. To correct this, a slight parallel shift of all ECA contours was performed along the major axis of the distal CCA contour. After that, a geometric model of the vessel and the computational grids on it were constructed. The grids were then exported to OpenFoam for numerical calculations.

For comparative analysis, geometric models m1–m10 were constructed using the method described above. Models m1–m9 simulate the results of CEA surgery on model m0 with p1–p9 patch implantation, respectively (Fig. 3). Model m10 (not shown in Fig. 3) simulates incision closure without patch implantation.

Data on patch shapes are given in Table 1, which contains the values of patch widths in their cross sections along the incision line. Point 0 in the "Distance..." column of the table corresponds to the proximal end of the incision line, point 3.9 to the distal end. The incision line shown in Fig. 1 (e) is the same for all models. Both its length 3.9 cm and location are same with the actual incision made during the classical CEA. The m10 model was constructed by reducing the circumference of the vessel lumen along the incision line. This is indicated by the negative values of the virtual patch width p10 in Table 1.

Note that Table 1 shows the incremental perimeter of the vessel after implantation, while the width of the patch itself before implantation should be somewhat greater.

Flow modeling

Flow velocity U and pressure p in the constructed geometric models were described using three-dimensional unsteady Navier-Stokes equations for a viscous incompressible fluid:

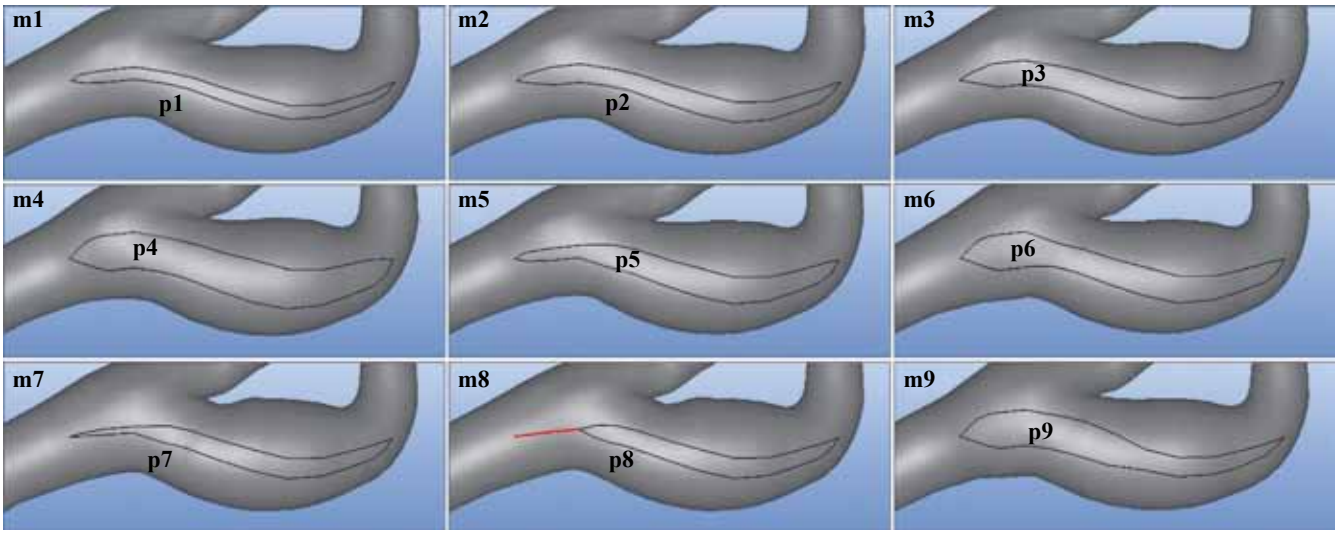

Fig. 3. Shapes of patches and vessels after virtual carotid endarterectomy

Table 1

The width (cm) of patches p1–p10 (cm) along the incision line

Distance along the cut (cm)	p1	p2	p3	p4	p5	p6	p7	p8	p9	p10
0.00	0.00	0.00	0.00	0.00	0.00	0.00	0.00	0.00	0.00	–0.00
0.29	0.12	0.16	0.19	0.34	0.13	0.35	0.05	–0.10	0.34	–0.26
0.72	0.14	0.21	0.28	0.42	0.14	0.42	0.07	0.00	0.42	–0.22
1.16	0.13	0.20	0.27	0.39	0.25	0.29	0.18	0.19	0.39	–0.22
1.59	0.14	0.20	0.27	0.40	0.27	0.27	0.20	0.20	0.38	–0.22
2.02	0.15	0.22	0.29	0.43	0.29	0.29	0.22	0.22	0.33	–0.24
2.46	0.16	0.24	0.33	0.47	0.33	0.33	0.24	0.24	0.24	–0.26
2.89	0.15	0.23	0.32	0.45	0.32	0.32	0.23	0.23	0.23	–0.26
3.32	0.13	0.20	0.27	0.39	0.27	0.27	0.20	0.20	0.20	–0.22
3.61	0.12	0.17	0.23	0.34	0.23	0.23	0.17	0.17	0.15	–0.14
3.90	0.00	0.00	0.00	0.00	0.00	0.00	0.00	0.00	0.00	0.00

$$\rho\left(\frac{\partial U}{\partial t}+(U\cdot\nabla)U\right)=-\nabla p+\nabla\tau,$$
$$\nabla U=0, \quad (1)$$

with constant density $\rho = 1050$ kg/m^3 and dynamic viscosity $\mu = 3.675 \times 10^{-3}$ Pa·s, where τ is shear stress tensor. The no-flow boundary condition was not set for U at the lateral surface of the flow area, but for parallel flow conditions at the inlet and outlet. The boundaries of the flow region were considered rigid. The initial velocity was chosen to be a constant 0.15 m/s. A periodically varying pressure difference was set as the boundary conditions for p at the inlet and outlets, which created a periodic flow corresponding to the patient's postoperative UDV data:

– T = 1.06 sec, cardiocycle period;
– Q = 6.9 mL/s, CCA volumetric flow rate;
– r = 1.72, ratio of CCA volumetric flow rate to ECA volumetric flow rate.

The method of constructing boundary conditions was as follows. First, a numerical calculation was performed in which both outputs were set to zero pressure, and a suitable pressure curve was plotted at the inlet step by step at 10 ms time intervals. During this calculation, the pressure increments at each time step were manually selected such that the resulting inlet velocity curve (see 4 (a)) corresponded to the UDV spectral envelope in the patient's CCA. Based on the results of this calculation, an *r* value was calculated that turned out to be different from the target value 1.72. Further, to correct the *r* value, a variable pressure, instead of zero, was set at the outputs. Namely, the same pressure curve was set at the ECA output as for CCA, only decreased in amplitude with coefficient $k = 0.1$ and with a slight phase lag. At the ICA output, the same pressure curve as at ECA was set, only inverted with respect to the x-axis. Thus, the ECA volumetric flow rate decreased, and ICA volumetric flow rate increased, while the CCA volumetric flow rate remained virtually unchanged. Then, with another series of auxiliary calculations, parameter *k* (and the shape of the pressure curve, if necessary) was corrected such that *Q* and *r* became close to their target values.

Numerical calculations and post-processing

Numerical calculations were performed in OpenFoam using the finite-volume method using the PISO algorithm, which along with commercial software such as Ansys Fluent, OpenFoam is a common tool for performing hydrodynamic calculations and simulating flow in blood vessels [4]. In the described preliminary numerical calculations performed to obtain a flow consistent with UDV data, coarse computational grids were used. After satisfactory results were obtained from preliminary calculations, final calculations on fine grids were carried out. The calculations yielded dynamic fields of pressure, velocity, and velocity gradient in the flow region for several cardiac cycles with time discretization in 10^{-2} s increments. Information about flow parameters and its derived characteristics was extracted from the calculation results by post-processing performed in ParaView Ayachit.

To verify these results, we investigated their independence on mesh pitch. It was found that the results do not change significantly when grids with a number of nodes greater than 5×10^5 are used. The grid cell size on the lateral surface was set equal to half the size of the cell inside the computational domain. This was done to increase the accuracy of calculation of hemodynamic indices, which are expressed through the velocity gradient on the vessel wall. Stabilization of periodic oscillations was also studied. As it turned out, the process of pulse oscillations can be considered stable starting from the second cardiac cycle [5]. In this connection, it is further assumed that time t = 0 corresponds to the beginning of the systolic increase in flow velocity in the second cardiac cycle.

Parietal shear stress and hemodynamic indices

The wall shear stress index (WSS) indicator was calculated as the tangential component t_w of shear stress tensor τ exerted on the vessel wall. The time average WSS (TAWSS), oscillatory shear stress (OSI) and relative residence time (RRT) indices were calculated according to formulas (2) through the averaged t_w value for one cardiac cycle [24]:

$$TAWSS=\frac{1}{T}\int_0^T\tau_w\,dt, \quad OSI=\frac{1}{2}\cdot\left(1-\frac{\left|\int_0^T\tau_w\,dt\right|}{\int_0^T|\tau_w|\,dt}\right),$$
$$RRT=\frac{T}{(1-2\cdot OSI)\cdot\int_0^T|\tau_w|\,dt}. \quad (2)$$

Here *T* is cardiac cycle duration, and $|t_w|$ is the Euclidean norm of vector t_w. To quantitatively compare the indices in some zone σ on the vessel wall, their average values were calculated according to the formulas:

$$RRT_\sigma=\frac{1}{s}\int_\sigma RRT\,d\sigma, \quad OSI_\sigma=\frac{1}{s}\int_\sigma OSI\,d\sigma,$$
$$TAWSS_\sigma=\frac{1}{s}\int_\sigma|TAWSS|\,d\sigma, \quad (3)$$

where S is the area of the zone σ. We also used the dimensionless mean I_RRT and logarithmic maximum M_RRT values of the RRT index for the zone σ, which were calculated using the formulas:

$$I\_RRT = TAWSS_{CCA} \cdot RRT_{\sigma},$$
$$M\_RRT = \max_{\sigma}(\ln(RRT \cdot TAWSS_{CCA} + 1)). \quad (4)$$

Here, $TAWSS_{CCA}$ is the averaged TAWSS value in the cylindrical part of the CCA at a distance of three CCA radii from the branching point of the vessel [24].

The TAWSS < 0.4 Pa and OSI > 0.3 inequalities given in Harrison (2014) [6] were used to assess pathological RRT values. In this case, formula (2) gives the corresponding critical value of RRT = 6.25 Pa^{-1}. Further, RRT values exceeding the critical value will be considered pathological.

RESULTS

Basic model flow results

The results of velocity field and hemodynamic calculations for baseline model *m*0 were analyzed. Fig. 4 shows some visualizations for the following parameter values: T = 1.06 s, Q = 6.9 mL/s, r = 1.72. Fig. 4 (a) shows a plot of the velocity vector modulus at the center of the CCA proximal cross section.

Table 2

Flow parameters T (s), Q (mL/s), r (dimensionless) in calculations a–d

	T	Q	r
a	1.06	6.90	1.72
b	1.06	6.00	1.78
c	0.7	7.76	1.77
d	0.8	10.65	1.72

Fig. 4 (b–d) respectively shows the current lines at time points t = 0.06 s, 0.14 s, and 0.6 s, which are marked with dots in Fig. 4 (a). The color changes along the current line reflect the velocity of the blood particles according to the scale provided.

We also studied the effect of pulse frequency and amplitude on distribution of hemodynamic indices on the vessel wall in the area of its atherosclerotic lesion. Table 2 shows the values of T, Q, and r for the four calculation variants, designated by letters a–d.

Fig. 5 (a–d) shows the RRT level lines on a selected section of the vessel wall corresponding to the same-name parameter sets from Table 2. Level 0 lines correspond to the critical value of RRT = 6.25 Pa^{-1}. Level 1–3 lines correspond to RRT values 2, 4 and 8 times greater, respectively, than the critical value. The color indicates the ln(RRT + 1) value between 0 and 8 according to the supplied scale. Fig. 7 shows the location of the selected site on the vessel wall. Fig. 5 (a–d) demonstrates that there is no significant qualitative change in the distribution of the RRT parameter when the flow parameters given in Table 2 are varied.

Fig. 6 shows a slightly enlarged view of the area of local maximums of the RRT index from Fig. 5 (a) in combination with the phase portrait of the TAWSS vector field.

The arrows in the figure indicate the local direction of the TAWSS field; the color reflects the ln(RRT + 1) value in the range [0, 8]. The black dots are fixed points of the TAWSS field, the bold lines are the separatrices of two saddle points 2 and 4, and the thin lines represent regular trajectories.

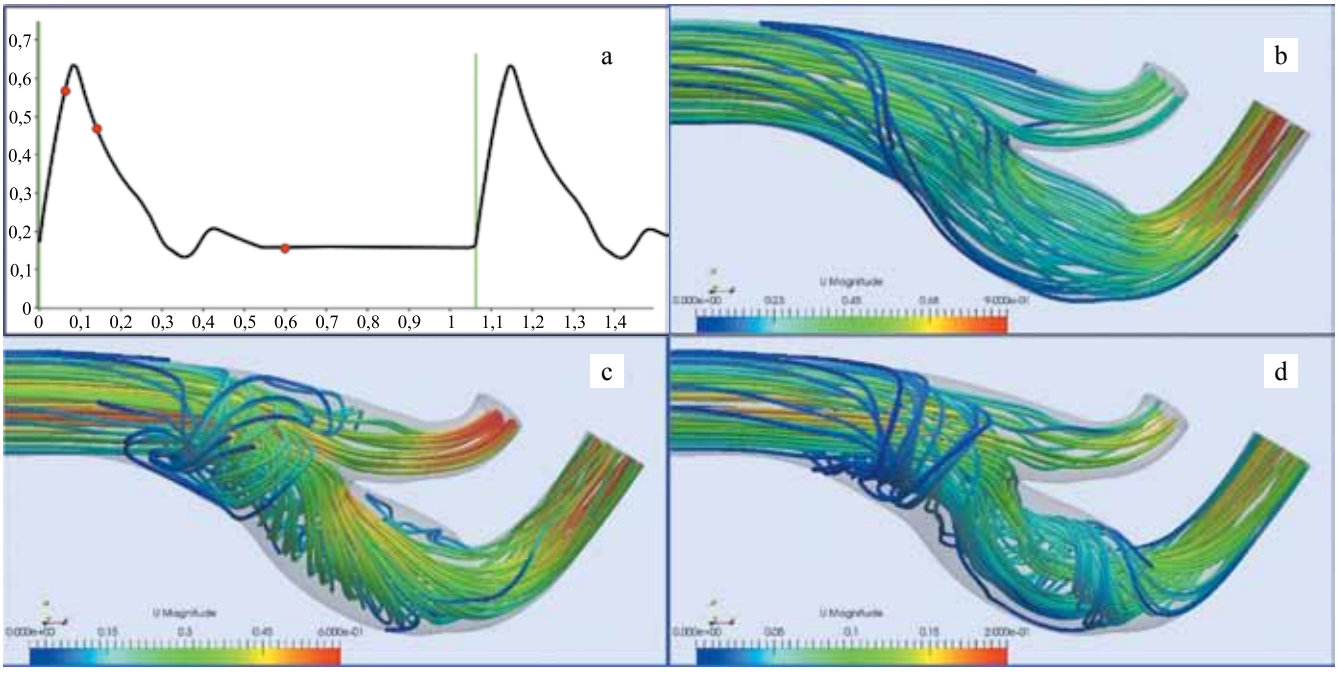

Fig. 4. Velocity plot for CCA (a). Streamlines at: t = 0.06 s (b), t = 0.14 s (c), t = 0.6 s (d)

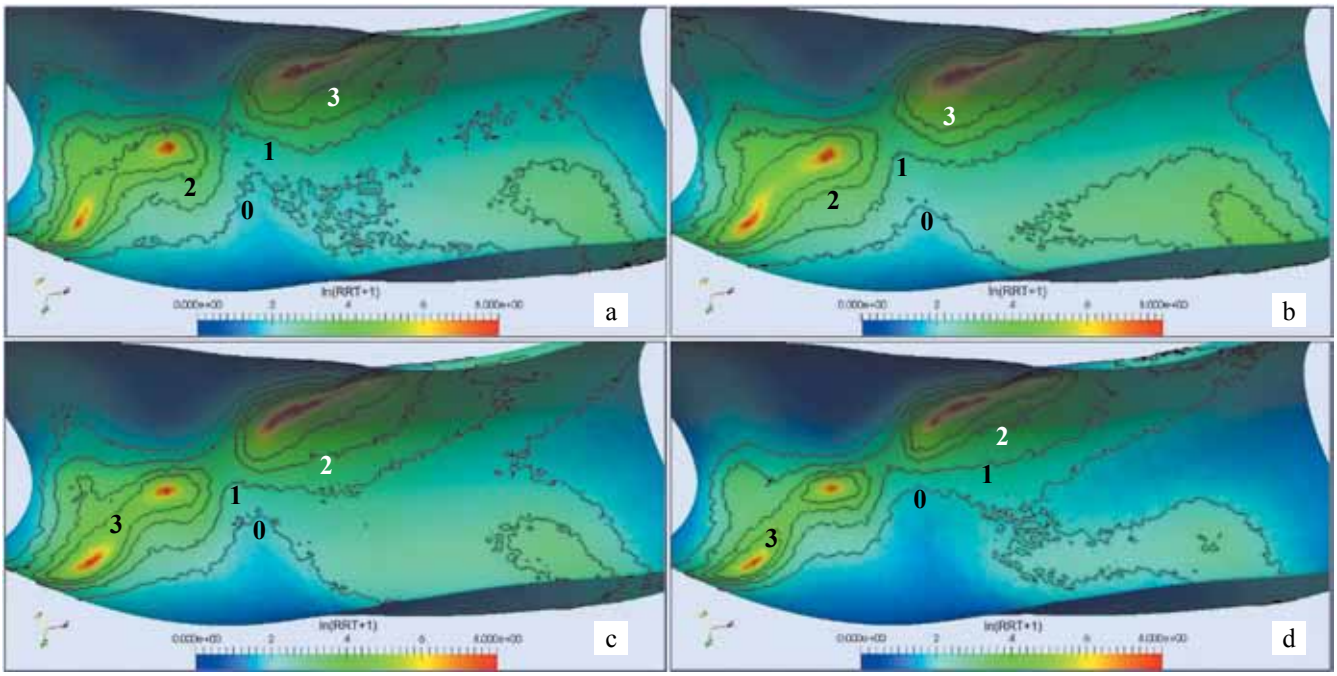

Fig. 5. RRT level lines (Pa^{-1}) and ln(RRT + 1) distribution for parameter sets a–d in Table 2

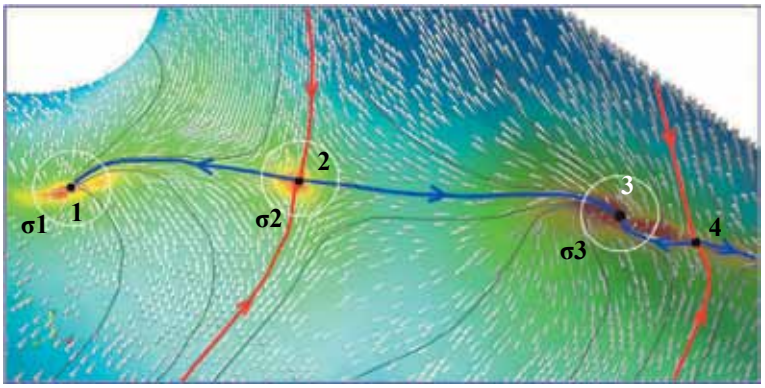

Fig. 6. Topological structure of the TAWSS field in the vicinity of its rest points (points 1–4)

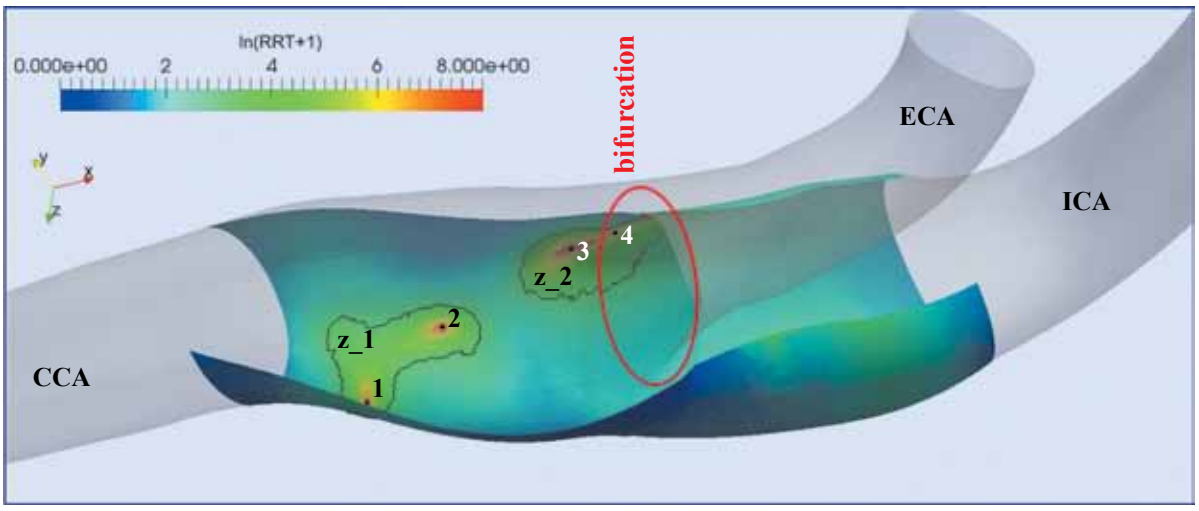

Fig. 7. z_1 and z_2 zones and stationary points 1–4 of the TAWSS field for the baseline model

Three zones σ1–σ3 (see Fig. 6) with equal areas *S* were chosen for comparative quantification of the integral RRT values. The centers of these zones are stationary points 1–3 of the TAWSS field. The average values of the indices calculated for each zone using formulas (3) are given in Table 3.

Hemodynamic indices for m0–m10 models

The results of numerical calculations with flow parameters *Q* and *r* differing by no more than 0.7% from calculation result "a" for the basic model (see Table 2) were obtained for models *m*1–*m*10. Changes in the geometric shape of the vessel caused by the virtual patch implantation causes changes (within 10%) in the calculated values of *Q* and *r* under unchanged boundary conditions. For this reason, auxiliary calculations were performed for each of the *m*1–*m*10 models in order to fit within the interval [–0.7%, 0.7%] of changes in *Q* and *r* parameters.

In order to obtain comparative quantitative characteristics of hemodynamic indices, regions were selected in each model where both criteria TAWSS < 0.4 Pa and OSI > 0.3 were simultaneously satisfied. These regions for all models consisted of two zones *z*_1 and *z*_2, the first containing stationary points 1, 2, and the second containing stationary points 3, 4 of the TAWSS field. Fig. 7 depicts these zones for the basic model. The I_RRT and M_RRT values in zones *z*_1 and *z*_2 calculated by formulas (4) for each model are shown in Table 4. The table rows show the I_RRT and M_RRT values for *m*0–*m*10 models as a percentage of the corresponding values for the baseline model m0.

Table 3

Average index values in zones

	RRT_σ (Pa^{-1})	$\ln(RRT_\sigma + 1)$	OSI_σ	$TAWSS_\sigma$ (Pa)
σ_1	287	5.66	0.409	0.047
σ_2	739	6.61	0.428	0.049
σ_3	974	6.88	0.453	0.031

Table 4

Comparison of I_RRT and M_RRT for m0–m10 models

	I_RRT_1	I_RRT_2	M_RRT_1	M_RRT_2
m0	100%	100%	100%	100%
m1	88.8%	97.8%	78.7%	98.7%
m2	78.6%	94.7%	75.9%	95.8%
m3	71.8%	92.9%	70.0%	96.1%
m4	76.1%	96.5%	74.3%	96.8%
m5	76.3%	96.8%	75.2%	98.3%
m6	75.4%	98.1%	82.5%	97.3%
m7	75.9%	97.3%	74.9%	99.8%
m8	75.7%	97.0%	74.2%	99.9%
m9	77.0%	95.7%	74.6%	98.3%
m10	82.0%	110.0%	81.9%	105.9%

DISCUSSION

Building geometric models

Our task was to reconstruct the segmentation of the original healthy vessel by computed tomography from angiography of the affected vessel. In intact vessel sections (Fig. 1 (b)), the lumen boundaries coincide with its inner wall, and segmentation in SimVascular can be performed automatically. However, in the areas of atherosclerotic lesions (Fig. 1 (c)) there is no such coincidence, so each contour was built using manual correction followed by Fourier smoothing. For example, the right side of the contour in Fig. 1 (c) was built on the outer border of the radiopaque calcified plaque. In addition, due to the limited resolution of the equipment, the vessel lumen boundary is blurred, hence, there is some scaling uncertainty when recognizing it. Therefore, the areas of some recognized cross sections were compared with the areas of the same cross sections obtained by UDV tools, a correction factor was calculated, and then all contours were scaled according to this factor. As a result, the CCA-ICA and ECA segmentations were obtained (Fig. 1 (d)), from which the baseline model *m*0 (Fig. 1 (e)) was constructed.

Flow modeling

Flow modeling was performed under the assumption that blood is a Newtonian fluid. It has long been established that non-Newtonian rheology manifests itself mainly in small-diameter vessels and capillaries. Therefore, Newtonian rheology is usually used to simulate flow in the carotid artery [7].

The assumption of a stiff vessel wall was accepted in this work for several reasons. First, a healthy carotid artery is located in a bed of elastic and pliable structures of connective and fatty tissue, within which its wall moves. With the appearance of calcified atherosclerotic plaque, pulse movements of the vessel wall in its area stop due to lack of flexibility. Plaque removal followed by patch implantation, however, does not fully restore the flexibility of the vessel wall, since the pliable surrounding structures are replaced by rigid connective tissue due to surgical trauma. Note that the absence of vascular wall movements in response to pressure changes inside the vessel from the medical point of view is the most unfavorable hemodynamic option, which was chosen in the work as the model with the worst prognosis. Secondly, the investigated sections of the vessel are much shorter than the pressure pulse wavelength. So, in the case of an elastic wall, we can assume that they expand and contract almost synchronously. Therefore, if we estimate the pulsation amplitude of the vessel diameter at 5%, the amplitude of oscillations of the peak WSS value will not exceed 15% [8]. However, for integral indices (2), this peak systolic value is averaged over the entire cardiocycle period and its effect on the indices will be

several times less. Finally, the introduction of additional input data required for calculations with a deformable wall, such as its mechanical properties and thickness into the model, require their accurate assessment. Otherwise, the assumed errors in these data may introduce uncontrollable uncertainty into the calculation results [8]. For these reasons, the assumption of wall stiffness is fairly common for the carotid artery.

Analysis of results for the m0 model

It is known that the flow in a carotid bifurcation has a complex structure; it always contains time-varying recirculation and stagnation zones [9]. In our case, the qualitative behavior of the streamlines depicted in Fig. 4 (b–d) corresponds to the published results.

To determine the probable position of atherosclerotic plaque initiation zones and their dependence on blood flow parameters, we obtained the distribution of hemodynamic indices (Fig. 5) for four calculation variants (Table 2). Fig. 5 shows that the location of the zones with high RRT values is almost independent of the changes in T and Q parameters.

Fig. 6 shows the phase portrait of the TAWSS vector field corresponding to the parameter set "a" from Table 2. In the considered area, the TAWSS field has four stationary points, marked in Fig. 6 by numbers 1–4. Points 1 and 3 are stable nodes, points 2 and 4 are saddle points (unstable). The arrows in Fig. 6 correspond to the direction of shear stress action on endothelial cells. The phase trajectories of the TAWSS field correspond to the transport pathways of blood components and chemicals along the vessel wall. Calculations performed also for the b–d parameter sets from Table 2 showed that the topological structure of the TAWSS vector field in the considered area is identical for all four a–d variants. This fact, together with the results shown in Fig. 5, allows us to conclude that changes in flow parameters have less influence on the configuration of the risk zones compared to changes in the geometric shape of the vessel.

Table 3 shows that in terms of worsening values of hemodynamic indices, the σ1–σ3 zones are arranged in the order of their numbering. Note that the location of the real atherosclerotic plaque in Fig. 1 (a), correlates with the location of risk zones σ1–σ3 in Fig. 6. Occurrence of the plaque changes the local hemodynamics, which leads to the spread of pathological areas and its further growth. Thus, it can be assumed that plaque formation in a healthy m0 vessel started from the special points of the TAWSS field. The vicinity of σ3, according to Table 3, all other things being equal, has the highest probability of pathological phenomena.

Comparative analysis of results for m0–m10 models

Comparative results of calculating I_RRT and M_RRT in z_1 and z_2 zones for all models are shown in Table 4. Zones z_1 and z_2 are the zones of the most likely occurrence of atherosclerotic phenomena; larger values of the indices in them mean a greater risk of restenosis. According to Table 1, p1–p4 patches have an approximately constant width along their entire length, except for the ends. These patches are the most commonly used by practicing surgeons, leaving the choice of patch width up to them. The world literature does not reveal any rules for the patch width in any particular case. However, the choice between patch implantation and incision closure without patch implantation is also discussed [10]. The data in Table 4 suggest that, in terms of risk of restenosis in both z_1 and z_2 zones, p3 is preferable among p1–p4 patches. The preference for using a patch before direct closure of the incision in our case is confirmed by the data in Table 4 for the m10 model simulating such an operation.

In this work, in contrast to those mentioned above, patches of unequal width were also investigated. As shown in Table 1, patches p5 and p6 were derived from patch p3 by narrowing and widening it proximally, respectively. Both variants lead to worser values in Table 4.

Patches p7 and p8 were derived from p2. The p7 patch is a p2 narrowed at its proximal end. The p8 is a p2 shortened by 0.7 cm, implanted in the incision, with direct closure of the incision in the proximal part with a 0.1 cm decrease in the vascular lumen circumference. In both cases, there was a slight improvement in the z_1 zone and deterioration in the z_2 zone compared to the p2 patch.

The p9 patch is derived from p4 by narrowing it distally, and this does not lead to any significant changes in the values in Table 4.

Thus, in our case, the best results are obtained with medium-width patches without narrowing or widening at the ends. The best option is to choose the p3 patch, and the worst option is to close the incision without a patch.

In summary, we should note the high prospect of the presented computer modeling method in personalized selection of an optimal patch for implantation into the arteriotomy. As previous studies have shown, this method makes it possible not only to calculate the deformation of hemodynamic indices in the carotid bifurcation, but also to predict the probability of restenosis development in a particular area [11–13]. In the future, the demonstrated method can become the basis for individual approach in choosing the patch size and shape, which will reduce the number of adverse cardiovascular events due to prevention of vessel lumen loss and recurrent strokes.

CONCLUSION

In the case under consideration, it was found that the width of the implanted patch, approximately equal to 3 mm, provides an optimal hemodynamic outcome. Deviations from this median value, either upward and downward, impair hemodynamics, and the absence of the patch gives the worst of the results considered. The proposed technique may assist in experimental selection of a patch.

The authors declare no conflict of interest.

REFERENCES

1. *Kazantsev AN, Tarasov RS, Burkov NN, Shabaev AR, Leader RYu, Mironov AV.* Carotid endarterectomy: three-year follow-up in a single-center registry. *Angiology and vascular surgery.* 2018; 24 (3): 101–108. [In Russ, English abstract].
2. *Kazantsev AN, Tarasov RS, Burkov NN, Volkov AN, Grachev KI, Yakhnis EYa et al.* Hospital results of percutaneous coronary intervention and carotid endarterectomy in hybrid and phased modes. *Angiology and vascular surgery.* 2019; 25 (1): 101–107. [In Russ, English abstract]. doi: 10.33529/angio2019114.
3. *Zhong L, Zhang JM, Su B et al.* Application of Patient-Specific Computational Fluid Dynamics in Coronary and Intra-Cardiac Flow Simulations: Challenges and Opportunities. *Front Physiol.* 2018; 9: 742. doi: 10.3389/fphys.2018.00742.
4. *Gijsen F, Katagiri Y, Barlis P et al.* Expert recommendations on the assessment of wall shear stress in human coronary arteries: existing methodologies, technical considerations, and clinical applications. *Eur Heart J.* 2019; 40 (41): 3421–3433. doi: 10.1093/eurheartj/ehz551.
5. *Borisov VG, Zakharov YN, Shokin YI et al.* Numerical Method for Predicting Hemodynamic Effects in Vascular Prostheses. *Numer Analys.* 2019; 12: 326–337. doi: 10.1134/S1995423919040025.
6. *Harrison GJ, How TV, Poole RJ, Brennan JA, Naik JB, Vallabhaneni SR, Fisher RK.* Closure technique after carotid endarterectomy influences local hemodynamics. *J Vasc Surg*. 2014; 60 (2): 418–427. doi: 10.1016/j.jvs.2014.01.069.
7. *Geers AJ, Morales HG, Larrabide I, Butakoff C, Bijlenga P, Frangi AF.* Wall shear stress at the initiation site of cerebral aneurysms. *Biomech Model Mechanobiol*. 2017; 16 (1): 97–115. doi: 10.1007/s10237-016-0804-3.
8. *Steinman DA.* Image-based computational fluid dynamics modeling in realistic arterial geometries. *Ann Biomed Eng.* 2002; 30 (4): 483–497. doi: 10.1114/1.1467679.
9. *Hoskins PR, Hardman D.* Three-dimensional imaging and computational modelling for estimation of wall stresses in arteries. *Br J Radiol.* 2009 Jan; 82 Spec No 1: S3–17. doi: 10.1259/bjr/96847348.
10. *Avrahami I, Raz D, Bash O.* Biomechanical Aspects of Closing Approaches in Postcarotid Endarterectomy. *Comput Math Methods Med.* 2018; 2018: 4517652. doi: 10.1155/2018/4517652.
11. *Kazantsev AN, Burkov NN, Zakharov YuN, Borisov VG, Lider RYu, Bayandin MS, Anufriev AI.* Personalized brain revascularization: a method of computer modeling of the reconstruction area for carotid endarterectomy. *Surgery.* 2020; (6): 71–75. [In Russ, English abstract]. doi: 10.17116/hirurgia202006171.
12. *Kazantsev AN, Burkov NN, Borisov VG, Zakharov YN, Sergeeva Tyu, Shabaev AR et al.* Computer modeling of hemodynamic parameters in the bifurcation of the carotid arteries after carotid endarterectomy. *Angiology and Vascular Surgery.* 2019; 25 (3): 107–112. [In Russ, English abstract]. doi: 10.33529/ANGIO2019311.
13. *Kazantsev AN, Vinogradov RA, Zakharov YN, Borisov VG, Chernyavsky MA, Kravchuk VN et al.* Prediction of restenosis after carotid endarterectomy by computer simulation. *Emergency medical care. Journal them. N.V. Sklifosovsky.* 2021; 10 (2): 401–407.doi: 10.23934/2223-9022-2021-10-2-401-407.

The article was submitted to the journal on 25.05.2020